PNAS RESEARCH ARTICLE | CHEMISTRY

Photoredox catalysis may be a general mechanism in photodynamic therapy

Mingle Li[a,1], Yunjie Xu[a,1], Zhongji Pu[b], Tao Xiong[c], Haiqiao Huang[c], Saran Long[c], Subin Son[a], Le Yu[a], Nem Singh[a], Yunkang Tong[c], Jonathan L. Sessler[d,2], Xiaojun Peng[c,2], and Jong Seung Kim[a,2]

Contributed by Jonathan L. Sessler; received June 23, 2022; accepted July 22, 2022; reviewed by Tomas Torres, Haiyan Xie, and Caixia Yin

Elucidating the underlying photochemical mechanisms of action (MoA) of photodynamic therapy (PDT) may allow its efficacy to be improved and could set the stage for the development of new classes of PDT photosensitizers. Here, we provide evidence that "photoredox catalysis in cells," wherein key electron transport pathways are disrupted, could constitute a general MoA associated with PDT. Taking the cellular electron donor nicotinamide adenine dinucleotide as an example, we have found that well-known photosensitizers, such as Rose Bengal, BODIPY, phenoselenazinium, phthalocyanine, and porphyrin derivatives, are able to catalyze its conversion to NAD^+. This MoA stands in contrast to conventional type I and type II photoactivation mechanisms involving electron and energy transfer, respectively. A newly designed molecular targeting photocatalyst (termed CatER) was designed to test the utility of this mechanism-based approach to photosensitizer development. Photoexcitation of CatER induces cell pyroptosis via the caspase 3/GSDME pathway. Specific epidermal growth factor receptor positive cancer cell recognition, high signal-to-background ratio tumor imaging (SBRTI = 12.2), and good tumor growth inhibition (TGI = 77.1%) are all hallmarks of CatER. CatER thus constitutes an effective near-infrared pyroptotic cell death photo-inducer. We believe the present results will provide the foundation for the synthesis of yet-improved phototherapeutic agents that incorporate photocatalytic chemistry into their molecular design.

photodynamic therapy | photoredox catalysis | NADH | pyroptosis

Significance

Elucidating the underlying mechanisms of action is vital to the development of improved photosensitizers for use in phototherapeutic cancer treatments (e.g., so-called photodynamic therapy). Here, we suggest that "photoredox catalysis in cells" might be a mechanistic determinant contributing to photodynamic therapy. CatER, a small molecule photocatalyst that absorbs in the near-infrared (NIR) spectral range, was prepared to test this hypothesis. Under conditions of NIR photoirradiation, CatER catalyzes the NADH/NAD^+ conversion, activates cell pyroptosis, and displays anticancer activity both in vitro and in vivo. We believe the present results highlight the utility of incorporating photoredox catalysis into photosensitizer design. As such, they set the stage for improvements in light-based cancer phototherapy.

Recent advances in light-driven catalysis have revolutionized the landscape of biology and medicine, allowing chemists to interrogate nature and develop various innovative biotechnologies (1–3). Appealing in this context is photodynamic therapy (PDT), which involves the synergistic use of light, a photosensitizer (PS), and molecular oxygen to generate reactive oxygen species (ROS) and damage malignant cells (4, 5). PDT is relatively noninvasive and, in principle, affords spatiotemporal control over the treatment process. Moreover, the photoactivated nature of PDT leads to toxicity patterns that circumvent the drug resistance pathways associated with many chemotherapeutics (4). Unfortunately, despite impressive advances in this area, the full clinical potential of PDT has yet to be realized. We believe that increased understanding of the mechanisms of action (MoA) underlying PDT could lead to improvements in PS design and ultimately a more-widespread adaptation of PDT as a cancer treatment modality. Here, we provide evidence in support of the notion that so-called "photoredox catalysis" constitutes a seemingly general contributory mechanism in PDT as underscored by (1) the study of several classic PDT PSs, and (2) the design and study of CatER, a small molecule photocatalyst that absorbs in the near-infrared (NIR) spectral region, activates cell pyroptosis, and demonstrates strong antitumor potency in a mouse model under conditions of NIR photoirradiation.

Historically, PDT effects have been considered to reflect two limiting MoA, namely type I and type II photosensitization reactions, as depicted in Fig. 1*A*, wherein the photoexcited PSs participate in electron (type I) or energy (type II) transfer process to produce cytotoxic ROS (5–8). However, recent reports have led to the suggestion that PDT may rely in part on different mechanistic pathways (9–12). Particularly relevant in this latter context is the pioneering work from Huang et al. (9), who demonstrated that the iridium complex [Ir(ttpy)(pq)Cl]PF_6 (see Fig. 1*C* for structure) could trigger a tandem photocatalysis process in cells that disrupts mitochondrial electron flow. This provides an alternative strategy for PDT within oxygen-poor environments, where the more classic type-II photosensitization pathway is restricted. Building on this finding, we recently reported an activatable photoredox catalytic approach (ConAPC) that provided for O_2-independent PDT within hypoxic tumors (12). In this report, we provide evidence that "photoredox catalysis in cells" could constitute a general contributory MoA in PDT that might not only (1) account in part for the efficacy of known

Author contributions: M.L., Y.X., J.L.S., X.P., and J.S.K. designed research; M.L., Y.X., Z.P., T.X., H.H., S.L., S.S., L.Y., N.S., and Y.T. performed research; M.L., Y.X., Z.P., T.X., H.H., S.L., S.S., L.Y., N.S., Y.T., J.L.S., X.P., and J.S.K. analyzed data; and M.L., J.L.S., X.P., and J.S.K. wrote the paper.

Reviewers: T.T., Autonoma University of Madrid; H.X., Beijing Institute of Technology; and C.Y., Shanxi University.

The authors declare no competing interest.

[1]M.L. and Y.X. contributed equally to this work.

[2]To whom correspondence may be addressed. Email: sessler@cm.utexas.edu or pengxj@dlut.edu.cn or jongskim@korea.ac.kr.

This article contains supporting information online at http://www.pnas.org/lookup/suppl/doi:10.1073/pnas.2210504119/-/DCSupplemental.

Published August 15, 2022.

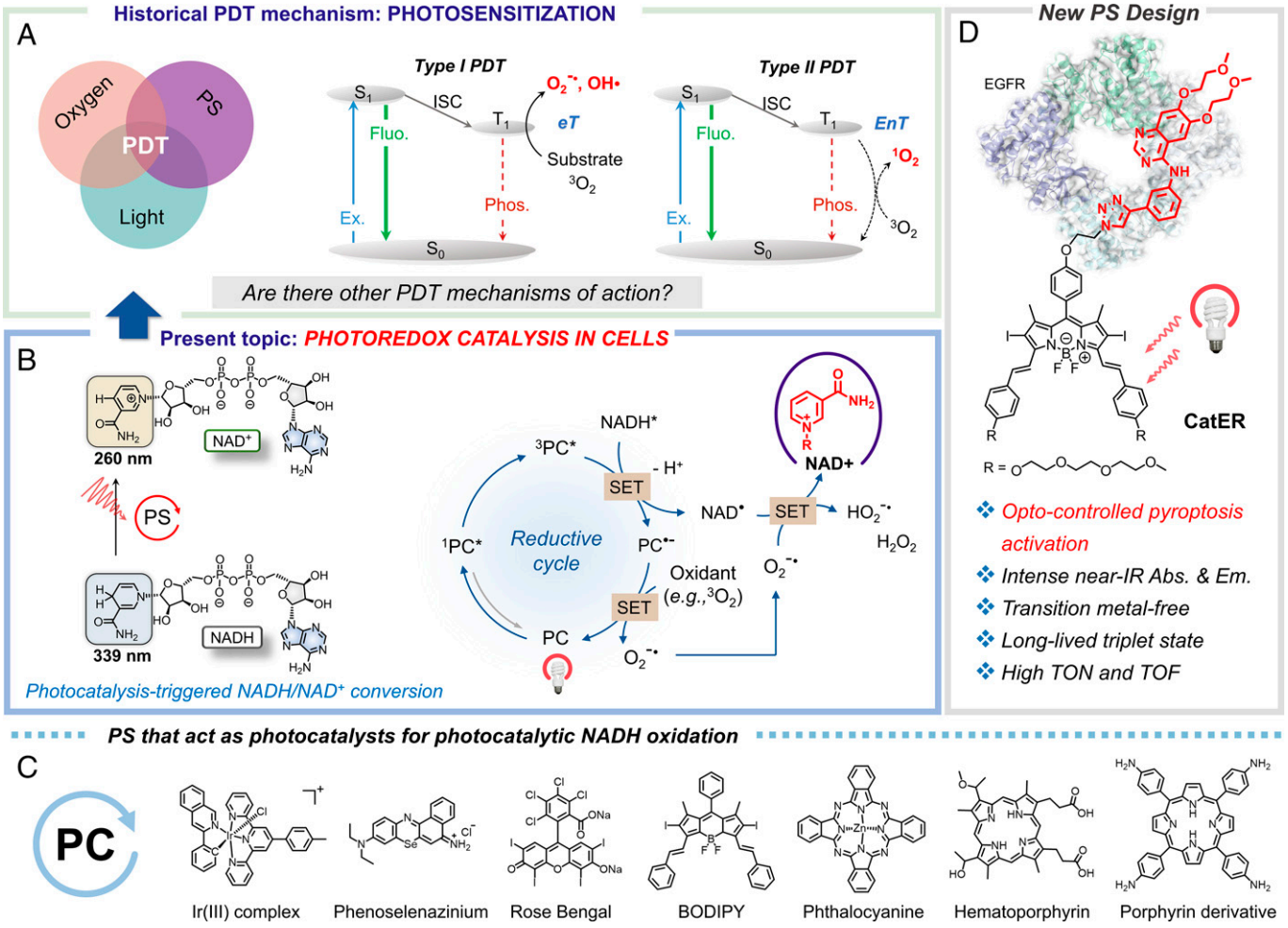

Fig. 1. Photodynamic therapy (PDT) mechanisms of action (MoA). (*A*) Schematic depicting the canonical PDT MoAs. (*B*) Photoredox catalysis MoA that is proposed to contribute to PDT effects in cells. *Left*: Proposed photocatalytic conversion of NADH to NAD^+ promoted by the combination of a PS and light. Characteristic absorption maxima of key subunits are also shown. *Right*: A plausible reductive quenching cycle involving photocatalytic NADH/NAD^+ conversion via a single electron transfer (SET) process. (*C*) Chemical structures of representative PSs whose MoA we suggest involves at least in part NADH photoredox catalysis. (*D*) Chemical structure and attributes of CatER, a molecular-targeting catalyst (MTcat) based on the tyrosine kinase inhibitor erlotinib. Abbreviations: S_0, group state; S_1, singlet excited state; T_1, triplet excited state; ISC, intersystem crossing; eT, electron transfer; EnT, energy transfer; PC, photoredox catalyst; SET, single electron transfer; Abs, absorption; Em, emission.

photosensitizers, but also (2) be exploited as a design principle for the construction of yet-improved PSs.

Nicotinamide adenine dinucleotide (NADH) (Fig. 1*B*) is a key reducing metabolite that plays a number of critical biochemical roles, including those associated with electron transfer (eT) within the respiratory electron transport chain (ETC) (13, 14). NADH also helps ensure proper cellular function; for instance, over 400 biocatalytic reactions in cells are dependent on NAD(P)H as the cofactor (15, 16). As such, photoredox-induced catalytic perturbations of the NADH/NAD^+ balance might be expected to induce metabolic dysfunction, thus contributing to a catalytic antitumor MoA that differs from classic type I and type II processes.

Most Food and Drug Administration (FDA)-approved and experimental PDT photosensitizers, representative examples of which are shown in Fig. 1*C*, are noted for absorbing in the far red or NIR spectral region where bodily tissues are relatively more transparent (17). In contrast, the seminal study of Huang et al. (9) noted above involved a system that required the use of blue-green light for activation. In fact, most photocatalysis systems currently under study in the broader context of synthetic methodology development operate in this spectral region (18). We thus (1) sought to test whether classic PS would induce NADH/NAD^+ conversion under conditions of photoirradiation and, if so, (2) whether the resulting knowledge could be parlayed into the development of a photoredox catalyst PS with tumor targeting or intrinsic cytotoxic capability. The present study was undertaken in an effort to address these questions.

As detailed below, we have found that several well-known photosensitizers, including Rose Bengal, BODIPY, phenoselenazinium, phthalocyanine, hematoporphyrin, and a tetraphenylporphyrin derivative are all able to trigger NADH/NAD^+ transformations via photoredox catalysis (Fig. 1*C* and *SI Appendix*, Scheme S1). To probe whether photoredox catalysis could be useful as a PS design principle, we have prepared a BODIPY-derived molecular targeting catalyst (MTcat), CatER, that incorporates the FDA-approved tyrosine kinase inhibitor erlotinib (ER) and tested whether it would allow for selective epidermal growth factor receptor positive ($EGFR^+$) tumor phototherapy (Fig. 1*D*). CatER functions within the more desirable NIR window. As detailed below, anticancer MoA investigations revealed that CatER generates single oxygen ($^1O_2$) effectively and induces NADH photoredox both in vitro and in vivo. Moreover, under conditions of photoirradiation, CatER induces gasdermin E (GSDME)-mediated pyroptosis, a recently characterized proinflammatory form of programmed cell death

(19, 20). Statistically significant tumor growth inhibition was also achieved in a murine cancer model.

Results and Discussion

Tests of Classic PDT Photosensitizers. Inspired by the report of Huang et al. (9) noted above, we began the present study by exploring whether known PS motifs would act as photocatalysts for a biologically relevant conversion. We chose NADH (180 μM) as the substrate for this study given its ubiquity and importance. We then selected several known PS, including Rose Bengal, BODIPY, phenoselenazinium (Se-NH_2), hematoporphyrin (HMME), phthalocyanine (ZnPc), and a porphyrin derivative (Por Ph-NH_2) (Fig. 1*C* for structures). Under conditions of photoirradiation, NADH was depleted and converted into NAD^+ in the presence of these representative PSs (5 μM), albeit with different efficiencies (Fig. 2*A*) as verified by the rapid absorbance decline at 339 nm (a spectroscopic signature of NADH), along with the absorbance increase at 260 nm (a spectroscopic signature of NAD^+) (21) (*SI Appendix*, Fig. S1). These findings led us to consider that photoredox catalysis might play a role in PDT. With the goal of testing whether this MoA is relevant in living systems, we optimized the BODIPY scaffold to obtain an NIR MTcat system (i.e., CatER) (Fig. 1*D*).

Design, Synthesis, and Photophysical Properties of CatER. CatER is a two component system containing ER and a BODIPY-type PS. ER is a FDA-approved tyrosine kinase inhibitor that has been widely used to target and inhibit EGFR (see Fig. 1 for a list of chemical abbreviations), which is overexpressed in multiple tumors, including lung, ovarian, head and neck cancers (22). The presence of ER is thus expected to provide CatER with desirable targeting and enhanced cytotoxicity. A parent molecule BDP without the ER moiety was prepared as a control (Fig. 2*B*). Detailed synthetic routes are provided in *SI Appendix*, Scheme S2. All compounds were characterized by ^{1}H NMR and ^{13}C NMR spectroscopy, ESI-HRMS, and high-performance liquid chromatography (HPLC) (*SI Appendix*, Figs. S2–S10). UV-visible spectrophotometry (UV-vis) studies revealed that CatER exhibits a typical Q-like band absorption in the 600–700 nm (ε = 65,042 $M^{-1} \times cm^{-1}$ at 660 nm, Fig. 2*C*) spectral range, as does BDP (*SI Appendix*, Fig. S11). Upon 660 nm excitation, an intense NIR fluorescence emission centered at 702 nm within the "biowindow" of 650–900 nm (23, 24) was observed for CatER. The absolute fluorescence quantum yield of CatER was determined to be 0.06. Nanosecond transient absorption (ns-TA) (Fig. 2*D*) difference spectral studies revealed that CatER could readily undergo intersystem crossing (ISC) to form the corresponding excited triplet state (T_1; i.e., ^{3}[CatER]*). The transient features of CatER matched well with those of BDP (*SI Appendix*, Fig. S12). On this basis, we conclude that the T_1 state of CatER is dominated by the BDP moiety rather than on the ER subunit.

Photocatalytic Conversion of NADH to NAD^+. In accord with our previous work (25), photoexcited CatER was found to generate $^1O_2$ effectively (Fig. 2*E*). It was thus expected that CatER could function as a PDT photosensitizer via a conventional type II MoA. However, a key goal of the present study was to determine whether CatER would also act as a PC capable of promoting the conversion of NADH into NAD^+. As shown in Fig. 2*F*, under conditions of photoirradiation (35 s, 660 nm laser, 100 mW/cm^2), NADH (180 μM in dimethyl sulfoxide

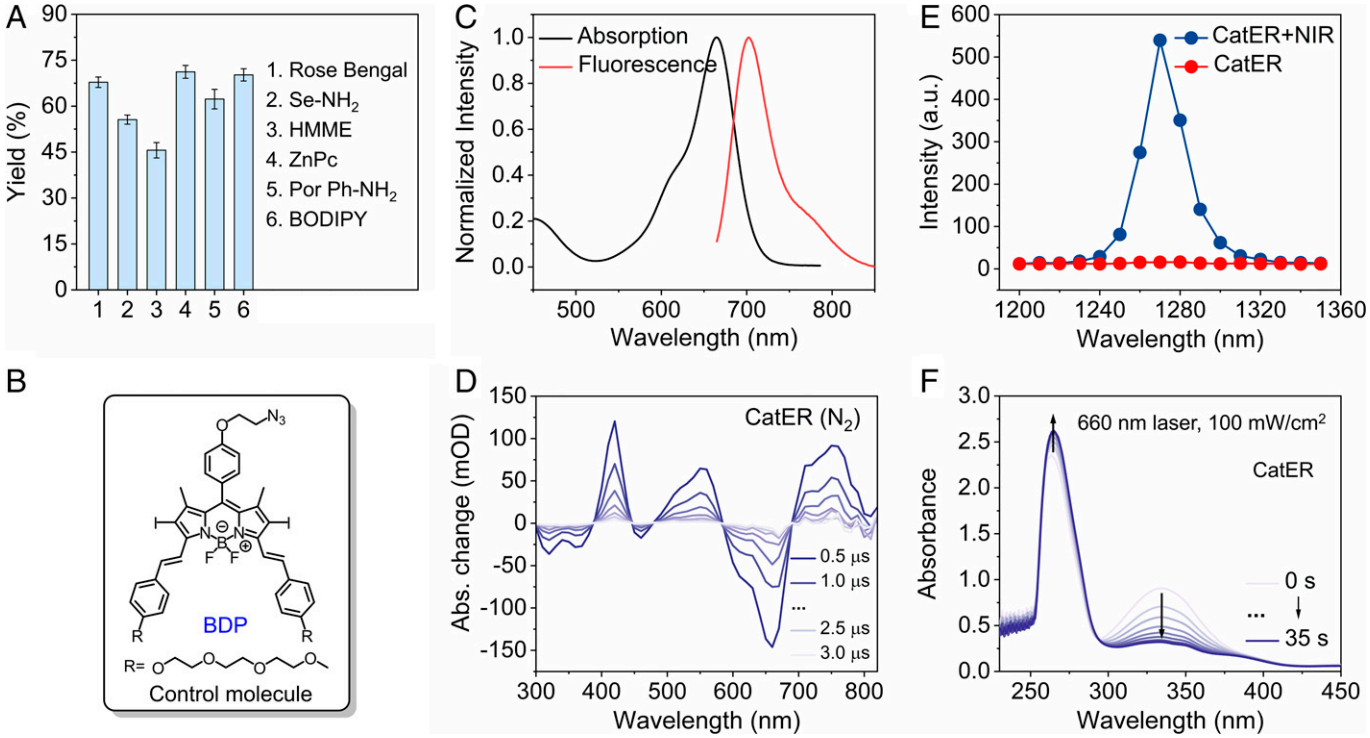

Fig. 2. Photophysical properties of CatER and studies of NADH/NAD^+ conversion. (*A*) Test of classic PDT PS motifs (5 μM), acting as photocatalysts for NADH/NAD^+ conversion. The yield is for NAD^+ produced after 35-s irradiation. Data are presented as mean ± SD, three independent tests. (*B*) Chemical structure of BDP. (*C*) Normalized absorption and emission spectra of CatER (5 μM) in DMSO. (*D*) Nanosecond transient absorption (ns-TA) difference spectra for CatER (5 μM) in deoxygenated CH_2Cl_2 at 293 K recorded using a LP980 ns-TA spectrometer under 570 nm pulsed excitation. (*E*) Emission spectra of CatER in air-saturated CH_2Cl_2 recorded in the presence and absence of photoirradiation. The emission centered around 1,270 nm is ascribed to $^1O_2$. (*F*) UV-vis spectra supporting the suggestion that the photocatalytic conversion of NADH (180 μM) to NAD^+ occurs under conditions of photoirradiation (660 nm laser, 100 mW/cm^2) in DMSO in the presence of CatER (5 μM).

[DMSO]) was converted into NAD^+ in the presence of CatER (5 μM) as inferred from UV-vis spectral studies. A plot of ln(Abs. at 339 nm) vs. irradiation time proved consistent with first-order reaction kinetics (*SI Appendix*, Fig. S13). Importantly, an $^1O_2$ quenching study using NaN_3 as an $^1O_2$ scavenger (26) (40 equiv. relative to CatER) revealed little appreciable change in the NADH depletion rate under otherwise identical conditions (*SI Appendix*, Fig. S14). This was taken as evidence that CatER-mediated photoredox catalysis constitutes the main mechanism underlying NADH photooxidation. Omitting CatER or light illumination from otherwise identical protocols resulted in no NAD^+ production (*SI Appendix*, Fig. S15).

In our hands, the maximal turn-over number (TON) and turn-over frequency (TOF) values for CatER NADH photocatalysis were found to be 28.75 and 49.3 min^{-1}, respectively; these values are higher (by ~3- to 100-fold) than those seen for common transition metal complexes and nanomaterials-based PCs (9, 27, 28). In the case of photoredox NADH catalysis, the SET process between the excited NADH* and the triplet state ^{3}[PC]* was identified as the rate-determining step for NADH/NAD^+ conversion (28). We therefore considered it likely that the relatively long excited-state lifetime of ^{3}[CatER]* (τ = 0.84 μs in N_2) (Fig. 3*A*) would abet this process. A favorable spatial interaction might also contribute to the high TON and TOF values. As can be seen from Fig. 3*B*, a density functional theory calculation revealed the formation of a relatively stable "clamped" complex between NADH and CatER. We thus propose that the corresponding excited triplet, ^{3}[CatER]*, is positioned close to the NADH electron-donor site allowing for electron transfer under conditions of photoexcitation.

In general, an intermediate form of catalyst needs to be converted back to its initial active form to complete the catalytic cycle (29). In the case of the putative photocatalyst CatER, electrons extracted from NADH need to be transferred to an electron acceptor (oxidant). In this study, dissolved O_2 was expected to fulfill this key function. To confirm this, we tested the photocatalytic performance of CatER under deoxygenated conditions. In contrast to the smooth NADH/NAD^+ conversion seen under air-saturated conditions, when a DMSO NADH solution was deaerated using N_2 almost no NAD^+ production was seen, with the calculated TOF being a mere 3.8 min^{-1} (Fig. 3*C* and *SI Appendix*, Fig. S16). On this basis, we conclude that O_2 is necessary to complete the catalytic cycle. Taking into account prior work (9), an O_2-dependent reductive quenching cycle operating via SET is thus proposed for the photoinduced conversion of NADH to NAD^+ in the presence of CatER (Fig. 1*B*).

Photoredox Catalysis in Cells. We next investigated the effect, if any, of the photoredox mechanistic paradigm in cell culture using A549 (human alveolar adenocarcinoma) cells. Per our design expectations, light dose-dependent depletion of NADH was seen. Specifically, ~23% decrease after 5 min irradiation and ~40% decrease after 15 min irradiation was observed for the CatER-treated cells (Fig. 4*B*). However, treatment with CatER in the dark had a negligible influence on the cellular NADH levels even after incubation for up to 24 h. As noted above, NADH and NAD^+ are not only crucial cofactors found in the cytoplasm (15, 16), but are also involved in many pathways related to cell metabolism, including the mitochondrial electron transport chain (mito-ETC) and glycolysis (Fig. 4*A*) (13, 14). We thus inferred that the photoredox catalysis-induced imbalance of NADH/NAD^+ would lead to significant changes in the cell function and cellular metabolic processes. Consistent with this supposition, it was found that when the A549 cells were treated with CatER in conjunction with photoirradiation (660 nm, 100 mW/cm^2), depolarization of the cellular mitochondrial membrane potential (MMP) was observed (*SI Appendix*, Fig. S17), indicating the loss of mitochondrial function integrity. Further support for this hypothesis came from the observation that formazan formation, a cellular redox reaction that requires NADH as a cofactor (16), was blocked (Fig. 4*C* and *SI Appendix*, Fig. S18).

Cell viability studies were then carried out using a standard water-soluble tetrazolium salt (WST-8) assay. Following light illumination (660 nm, 100 mW/cm^2, 5 min), both CatER and BDP (but not ER) exhibited a high level of antiproliferation activity in A549 cells and in a dose-dependent manner (Fig. 4*D*). The half-maximal inhibitory concentration (IC_{50}) was calculated to be approximately 0.4 and 0.7 μM for CatER and BDP, respectively. These photocytotoxicities are competitive with clinical available PSs, e.g., hematoporphyrin derivative HMME (IC_{50} >4.8 μM, *SI Appendix*, Fig. S19). Confocal imaging of live/dead cells using AM/PI double staining kit provided further support for the inferred phototherapeutic potency of CatER (*SI Appendix*, Fig. S20). Photosensitization-induced ROS generation for CatER was seen in A549 cells (*SI Appendix*, Fig. S21). In an effort to parse out the effects of ROS generation vs. photoredox catalysis, an analogous study was carried out in the presence of a large excess of NAC [*N*-acetyl-$_L$-cysteine, a ROS scavenger (30)]. Under these conditions, appreciable cell death was still observed (>43% vs. ~70% in the absence of NAC) (*SI Appendix*, Fig. S22). This was taken as support for the core contention that photoredox catalysis contributes, at least in

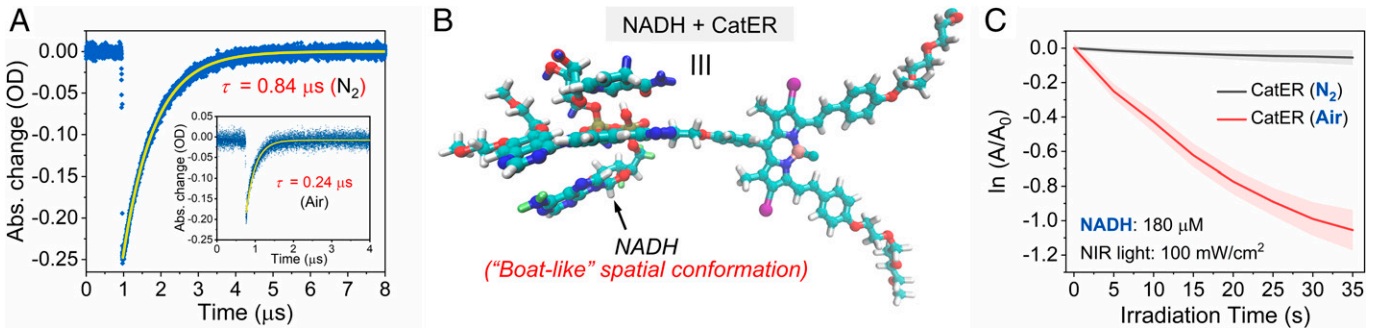

Fig. 3. Excited state studies. (*A*) Nanosecond time-resolved transient absorption decay traces at 660 nm for CatER recorded using a LP980 ns-TA spectrometer under 570 nm pulsed excitation (1 Hz, full width at half maximum ~ 7 ns), concentration = 5 μM in CH_2Cl_2, 293 K. (*B*) Optimized conformation of the complex presumed to be formed between CatER and NADH as deduced from density functional theory calculations. (*C*) Time-dependent absorbance change in the NADH absorbance at 339 nm seen in the presence of CatER (5 μM) under conditions of photoillumination in both air-saturated and deoxygenated DMSO solution.

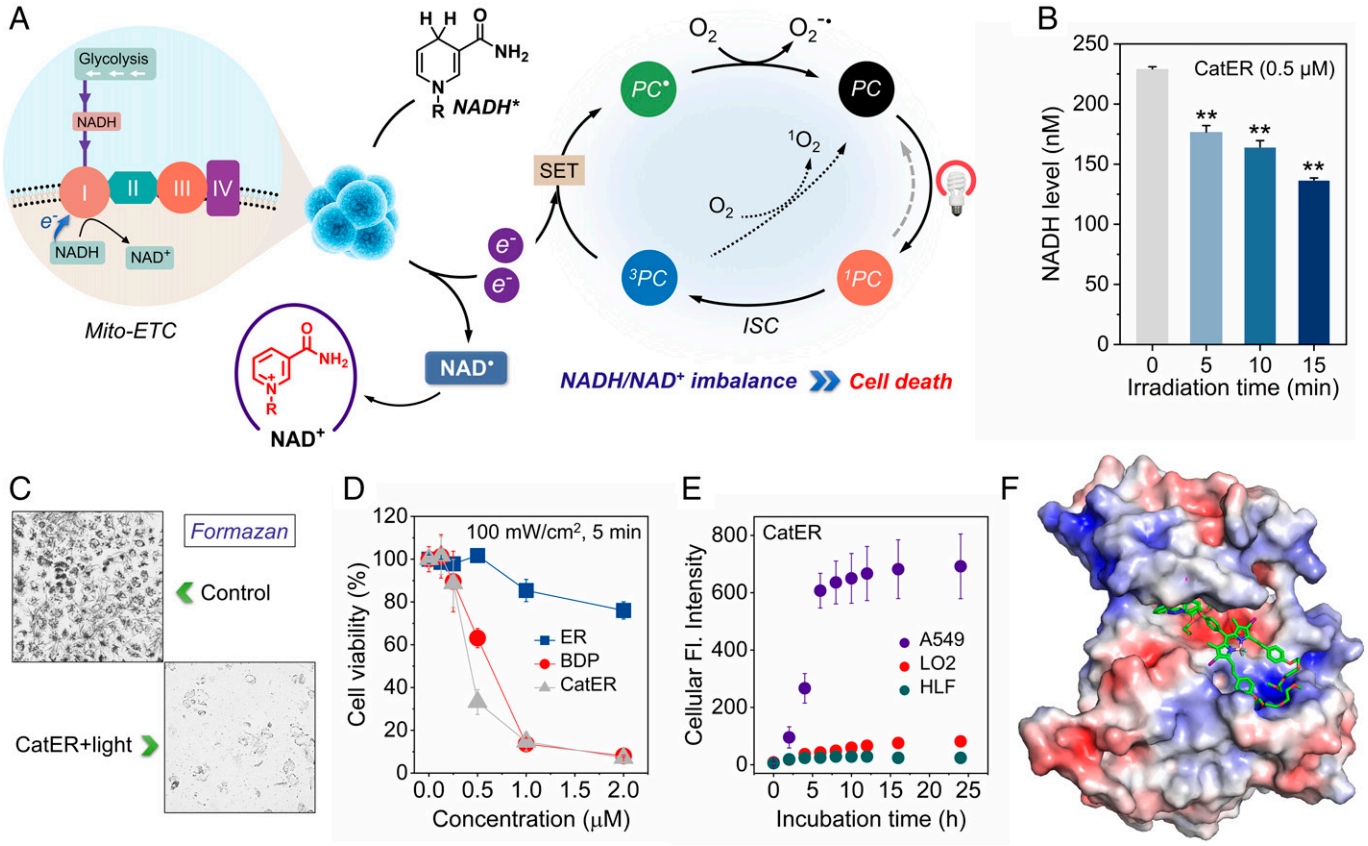

Fig. 4. Photoredox catalysis in cells and selective anticancer effects. (*A*) Schematic showing the proposed photoredox catalysis-induced disruption of the mitochondrial electron transport chain (mito-ETC) and metabolism resulting from NADH/NAD$^+$ imbalance. (*B*) Cellular NADH levels in A549 cells after treatment with 0.5 μM CatER and subjected to photoirradiation for various times (660 nm, 100 mW/cm^2). (*C*) Formazan formation in A549 cells. Light irradiation: 660 nm, 100 mW/cm^2, 5 min. (*D*) Cell viability of A549 cells subject to different treatment protocols. (*E*) Comparison of cellular uptake of CatER (1 μM) in EGFR$^+$ A549, EGFR$^-$ LO2 and HLF cells, as determined by cellular fluorescence intensity. (*F*) Proposed molecular docking of CatER into the pocket of EGFR. Data are presented as mean ± SD, three independent tests, $^{**}P < 0.01$.

part, to the overall PDT effect seen for CatER and by inference other PDT PSs.

Selective PDT toward EGFR$^+$ Cancer Cells. In accord with our design expectations, selective EGFR$^+$ cancer cell recognition and permeability were seen with CatER. For instance, at 24 h postincubation, the cellular fluorescence intensity ascribed to CatER in EGFR$^+$ A549 cells was approximately 8- and 29-fold higher than that in EGFR$^-$ LO2 (normal human hepatocyte) and HLF (normal human lung fibroblasts) cells, respectively (Fig. 4*E*). However, when the A549 cells were pretreated with an EGFR inhibiter (i.e., ER), the overall cellular uptake of CatER was inhibited in a statistically significant manner (*SI Appendix*, Fig. S23). This supports the inference that the observed selectivity was a direct consequence of active EGFR targeting. Selective ablation of EGFR$^+$ cancer cells was also achieved using CatER in conjunction with photoirradiation (*SI Appendix*, Fig. S24). By contrast, no such salutary outcome was seen for BDP (a control lacking the ER targeting moiety) (*SI Appendix*, Figs. S23 and S24).

Based on molecular docking studies (Fig. 4*F*), we propose that CatER docks effectively into the natural hydrophobic pocket of EGFR tyrosine kinase (PDB: 1M17). This docking appears thermodynamically favored. The binding free energy was calculated to be approximately −8.2 kcal/mol. Interactions, including hydrophobic (residues: Leu694, Phe699, Val702, Lys721, Leu820, Pro853, and Lys889) and π-π donor-acceptor effects (residue: Trp856) between the CatER backbone and the EGFR-TK domain, are thought to provide the driving force for binding (*SI Appendix*, Fig. S25). In contrast to free ER (the EGFR inhibitor subunit incorporated into CatER), an additional hydrogen bond at the residue Lys855 is seen in the case CatER (note that both systems provide for two hydrogen bonds, to residues Lys721 and Thr766) (*SI Appendix*, Fig. S25). Collectively, these results provide a rationale for the effective EGFR targeting seen in the case of CatER.

Cancer Cell Pyroptosis via Gasdermin E. In probing the cell death mechanism, we found that CatER PDT triggers gasdermin E (GSDME, a pore-forming protein)-mediated pyroptosis, a lytic and proinflammatory form of programmed cell death that is distinct from conventional cell apoptosis and necrosis (19, 20). Confocal laser scanning microscopy (CLSM) revealed morphologic changes in A549 cells upon CatER PDT that were consistent with pyroptosis. Specifically, after being cultured with 0.5 μM CatER and subjecting to photoirradiation (660 nm, 100 mW/cm^2, 5 min) obvious cell swelling, central localization of the nuclei (Fig. 5*A*), and bubble-like protrusions formation termed pyroptotic bodies (31) (as visualized by green fluorescence staining with Annexin V-fluorescein isothiocyanate (FITC) conjugate, white arrow; Fig. 5*B*) were seen for the A549 cells. Staining with Hoechst 33342 (blue fluorescence, Fig. 5*B*) revealed that the nucleus of A549 cells remained intact after CatER PDT, rather than undergoing fragmentation; this is a clear difference in morphology compared to apoptosis (32).

Further support for the suggestion that CatER PDT induces cell pyroptosis came from studies of N-terminal pore-forming

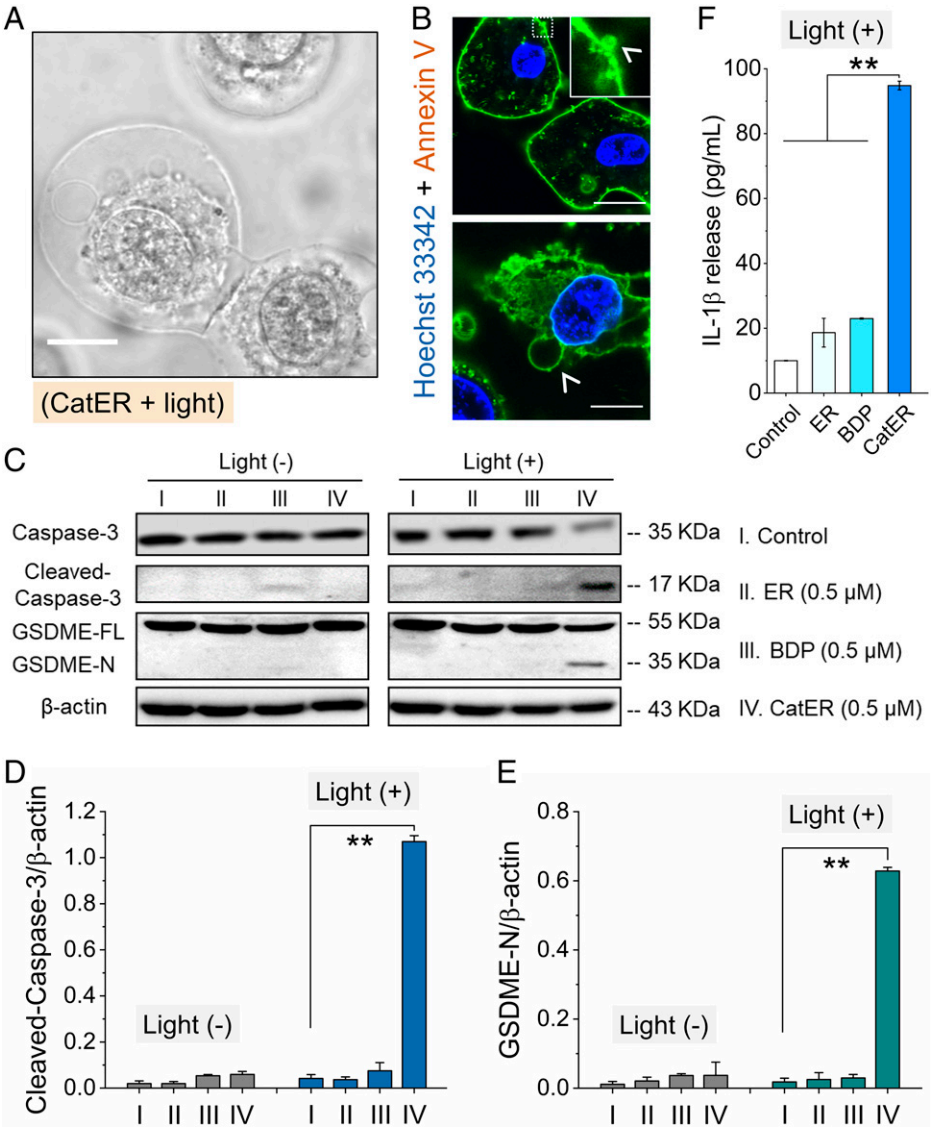

Fig. 5. CatER-initiated pyroptosis activation. (*A*) Confocal laser scanning microscopy images showing the cell morphological changes in A549 cells seen after treatment with 0.5 μM CatER with photoirradiation (660 nm, 100 mW/cm^2, 5 min). (Scale bars: 10 μm.) (*B*) Confocal images of Annexin-V-FITC-positive budding vesicles in A549 cells (the nucleus was labeled using Hoechst 33342). (Scale bars: 10 μm.) Experimental conditions were identical to those of (*A*). (*C*) Western blots used for pyroptosis-related protein detection. Statistical analysis of cellular (*D*) cleaved caspase-3 and (*E*) GSDME-N protein expression; values derived from (*C*). (*F*) IL-1β release in A549 cells seen for the indicated treatments, concentration = 5 μM. Light: 660 nm, 100 mW/cm^2, 5 min. Data are presented as mean ± SD from three independent tests, $^{**}P < 0.01$.

domain GSDME-N activation as measured by a Western blot assay in A549 cells. As shown in Fig. 5 *C–E*, after exposure to CatER and subjecting to photoirradiation (660 nm, 100 mW/cm^2, 5 min), the expression level of cleaved-caspase-3 and cleaved-GSDME (i.e., GSDME-N) was increased. These observations are consistent with a previous report that cleaved caspase-3 can directly promote the cleavage of GSDME (19). The release of intracellular lactate dehydrogenase (LDH) (*SI Appendix*, Fig. S26) and proinflammatory cytokines interleukin (IL)-1β (Fig. 5*F*), two hallmarks of pyroptosis (33), was also seen. However, under otherwise identical conditions, no evident pyroptosis activation was seen with BDP. We ascribe this result to the fact that this control system lacks the ER subunit present in CatER. This limits cellular uptake and results in a low level of intracellular NADH/NAD$^+$ conversion (*SI Appendix*, Fig. S27). The relatively low level of cellular ROS generation of BDP could also contribute to this difference (*SI Appendix*, Fig. S28). In the absence of photoirradiation, no cells exhibited pyroptotic effects. On the other hand, no evidence of cell apoptosis (*SI Appendix*, Fig. S29*A*) or ferroptosis (*SI Appendix*, Fig. S29*B*) was seen in the case of CatER-mediated PDT under conditions identical to those that trigger pyroptosis. Taken in concert, these results support the proposition that CatER acts to induce pyroptosis under conditions of photoirradiation. As such, we propose that it, or other photoredox catalyst systems could find application as opto-controlled pyroptosis-inducing agents.

In Vivo NIR Imaging-Guided Anticancer Phototherapy. As a test of the potential of CatER to serve as a potential anticancer agent, we examined its ability to retard tumor growth in EGFR$^+$ 4T1 tumor-bearing Balb/c mice. As a prelude to these studies, the in vivo behavior of CatER was first explored using a small animal fluorescence imaging system. As shown in Fig. 6*A*, in contrast to what is seen in the case of BDP, 1 h after the intravenous (i.v.) tail vein injection of CatER, the tumor site was seen to "light up" and thus be readily distinguished from neighboring tissues. Over time, the NIR fluorescence signal of CatER in the tumor region was seen to increase gradually,

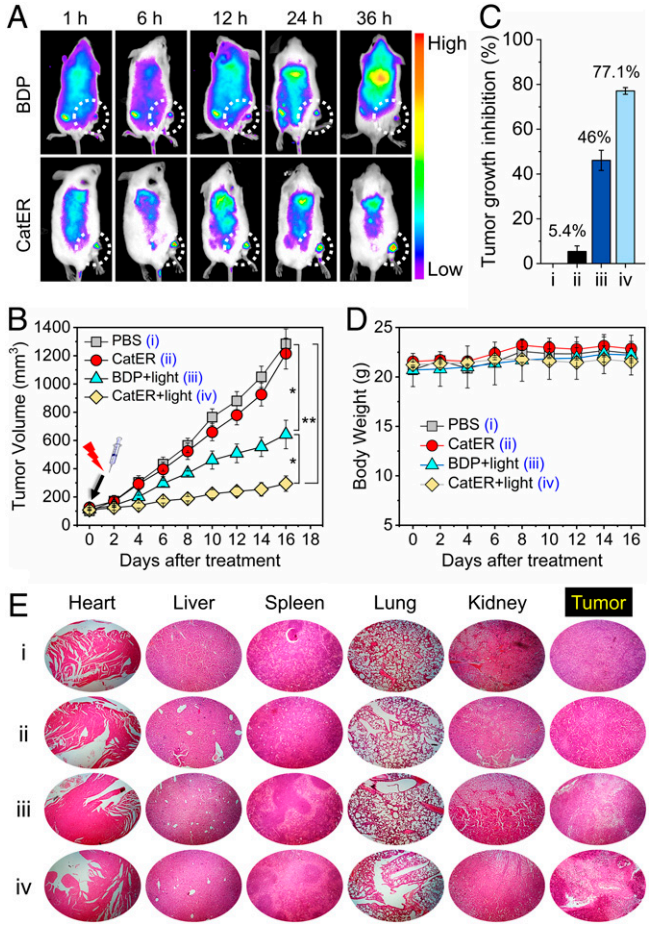

Fig. 6. PDT in vivo. (*A*) In vivo NIR fluorescence images of Balb/c mice bearing 4T1 tumors recorded at different time points after administering BDP or CatER i.v. (20 nmol in 200 μL PBS). (*B*) In vivo tumor growth curves for mice receiving different treatments (denoted as i–iv), including photoirradiation (660 nm laser, 100 mW/cm^2, 20 min) or no light. (*C*) Tumor growth inhibition (TGI) 16 d after various treatments. (*D*) Average body weights of tumor-bearing mice subject to different 16-d treatments. (*E*) H&E staining for pathological analysis of main organs and tumor tissue. Data are presented as mean ± SD, $n = 5$. *$P < 0.05$, **$P < 0.01$.

reaching a maximum 24 h postinjection. At this time point, a signal-to-background ratio (SBR) as high as 12.2 was obtained [SBR values ≥2.5 are regarded as preferential tumor accumulation (34)]. Moreover, ex vivo imaging revealed that CatER was rapidly excreted throughout most organs but retained preferentially in tumor tissues for >36 h as determined by fluorescence imaging (*SI Appendix*, Fig. S30). In contrast, no apparent tumor accumulation was noted for the control BDP (SBR: 1.68) (Fig. 6*A* and *SI Appendix*, Fig. S31), a finding ascribed to its lack of specific recognition for EGFR.

Antitumor treatment efficacy was then assessed. These studies revealed that 16 d after initial treatment, the tumor growth in the group of CatER + light was suppressed, with an average tumor growth inhibition (TGI) of ∼77% being recorded (Fig. 6 *B* and *C*), while for the BDP + light group, ∼50–60% of the tumor volume remained. Essentially no tumor inhibition was seen for CatER in the absence of photoirradiation or for the PBS control. Histological analysis of tumor slices using hematoxylin/eosin (H&E) staining provide further support for the conclusion that the combination of CatER and light acts to damage the tumor cells in vivo (Fig. 6*E*). Moreover, over the course of the present therapeutic studies, all mice behaved normally without any signs of stress or discomfort. No abnormal weight loss (Fig. 6*D*) and no apparent inflammation response in the main organs, including the heart, liver, spleen, lung, and kidneys, were observed (Fig. 6*E*). Collectively, these results are fully consistent with the in vitro anti-proliferation studies discussed above and provide support for the conclusion that CatER represents an effective NIR photocatalyst that may be used to suppress tumor growth in vivo.

Conclusion

In summary, we suggest that "photoredox catalysis in cells" might be a potential hidden MoA contributing to PDT effects. Screening studies of conventional PSs provided support for the notion that they mediate their function, at least in part, by acting as photoredox catalysts and disrupting cellular NADH homeostasis. To support this hypothesis, we designed and synthesized an NIR molecular targeting photocatalyst, CatER. Upon photoirradiation, CatER was found to promote photocatalytic NADH/NAD$^+$ conversion while providing for selective EGFR$^+$ cancer cell recognition. In vitro studies revealed that CatER in concert with NIR irradiation induces pyroptosis via caspase 3/GSDME. Finally, cancer cell ablation in vitro and tumor growth inhibition was demonstrated in vivo using a mouse model. Based on the present findings, we believe that photoredox catalysis may (1) represent a generalizable mechanism of action, and (2) an appreciation of its role in PDT may allow for the design of yet-improved phototherapeutics. The observation that CatER appears to induce pyroptosis in vitro is noteworthy in this regard. Pyroptosis has emerged as a new frontier in cancer research and is promising in the context of tumor immunotherapy. Specifically, we suggest that CatER or other PSs may have a role to play in stimulating tumor immunity via photo-induced pyroptosis activation. Work along these lines is currently ongoing in our group.

Materials and Methods

All reagents and assay kits used in this study are commercially available and used directly without purification. Experimental protocols including cell culture, confocal imaging, living animals, as well as the details of experimental instruments are described in SI Appendix.

Date Availability. All study data are included in the article and/or *SI Appendix*.

ACKNOWLEDGMENTS. We gratefully acknowledge financial support from the National Research Foundation of Korea (CRI project 2018R1A3B1052702 to J.S.K.), the National Natural Science Foundation of China (Project 22090011), and NSFC-Liaoning United Fund (U1908202). We also thank the Brain Pool Program administered through the National Research Foundation of Korea (NRF) (2020H1D3A1A02080172 to M.L.) for financial support. The work in Austin was supported by the Robert A. Welch Foundation (F-0018 to J.L.S.).

Author affiliations: [a]Department of Chemistry, Korea University, Seoul 02841, Korea; [b]Hangzhou Global Scientific and Technological Innovation Center, Zhejiang University, Hangzhou 311200, China; [c]State Key Laboratory of Fine Chemicals, Dalian University of Technology, Dalian 116024, China; and [d]Department of Chemistry, University of Texas at Austin, Austin, TX 78712-1224

1. K. A. Ryu, C. M. Kaszuba, N. B. Bissonnette, R. C. Oslund, O. O. Fadeyi, Interrogating biological systems using visible-light-powered catalysis. *Nat. Rev. Chem.* **5**, 322–337 (2021).
2. J. B. Geri *et al.*, Microenvironment mapping via Dexter energy transfer on immune cells. *Science* **367**, 1091–1097 (2020).
3. R. C. Oslund *et al.*, Detection of cell-cell interactions via photocatalytic cell tagging. *Nat. Chem. Biol.* **18**, 850–858 (2022).
4. P. Agostinis *et al.*, Photodynamic therapy of cancer: An update. *CA Cancer J. Clin.* **61**, 250–281 (2011).

5. S. Kwiatkowski *et al.*, Photodynamic therapy – mechanisms, photosensitizers and combinations. *Biomed. Pharmacother.* **106**, 1098–1107 (2018).
6. M. Li *et al.*, Unimolecular photodynamic O_2-economizer to overcome hypoxia resistance in phototherapeutics. *J. Am. Chem. Soc.* **142**, 5380–5388 (2020).
7. M. Li *et al.*, Near-infrared light-initiated molecular superoxide radical generator: Rejuvenating photodynamic therapy against hypoxic tumors. *J. Am. Chem. Soc.* **140**, 14851–14859 (2018).
8. M. Li *et al.*, Superoxide radical photogenerator with amplification effect: Surmounting the achilles' heels of photodynamic oncotherapy. *J. Am. Chem. Soc.* **141**, 2695–2702 (2019).
9. H. Huang *et al.*, Targeted photoredox catalysis in cancer cells. *Nat. Chem.* **11**, 1041–1048 (2019).
10. C. Huang *et al.*, In-vitro and in-vivo photocatalytic cancer therapy with biocompatible iridium(III) photocatalysts. *Angew. Chem. Int. Ed. Engl.* **60**, 9474–9479 (2021).
11. J. Sun *et al.*, Cascade reactions by nitric oxide and hydrogen radical for anti-hypoxia photodynamic therapy using an activatable photosensitizer. *J. Am. Chem. Soc.* **143**, 868–878 (2021).
12. M. Li *et al.*, Conditionally activatable photoredox catalysis in living systems. *J. Am. Chem. Soc.* **144**, 163–173 (2022).
13. D. V. Titov *et al.*, Complementation of mitochondrial electron transport chain by manipulation of the NAD^+/NADH ratio. *Science* **352**, 231–235 (2016).
14. C. Cantó, K. J. Menzies, J. Auwerx, NAD(+) metabolism and the control of energy homeostasis: A balancing act between mitochondria and the nucleus. *Cell Metab.* **22**, 31–53 (2015).
15. R. P. Goodman *et al.*, Hepatic NADH reductive stress underlies common variation in metabolic traits. *Nature* **583**, 122–126 (2020).
16. A. Chiarugi, C. Dölle, R. Felici, M. Ziegler, The NAD metabolome–a key determinant of cancer cell biology. *Nat. Rev. Cancer* **12**, 741–752 (2012).
17. X. Li, J. F. Lovell, J. Yoon, X. Chen, Clinical development and potential of photothermal and photodynamic therapies for cancer. *Nat. Rev. Clin. Oncol.* **17**, 657–674 (2020).
18. J. M. Narayanam, C. R. Stephenson, Visible light photoredox catalysis: Applications in organic synthesis. *Chem. Soc. Rev.* **40**, 102–113 (2011).
19. Y. Wang *et al.*, Chemotherapy drugs induce pyroptosis through caspase-3 cleavage of a gasdermin. *Nature* **547**, 99–103 (2017).
20. P. Yu *et al.*, Pyroptosis: Mechanisms and diseases. *Signal Transduct. Target. Ther.* **6**, 128 (2021).
21. J. W. H. Burnett, R. F. Howe, X. Wang, N. A. D. Cofactor, (P)H regeneration: How selective are the reactions? *Trends Chem.* **2**, 488–492 (2020).
22. B. Li *et al.*, Tumor inhibition achieved by targeting and regulating multiple key elements in EGFR signaling pathway using a self-assembled nanoprodrug. *Adv. Funct. Mater.* **28**, 1800692 (2018).
23. Y. Xu *et al.*, 2D-ultrathin MXene/DOXjade platform for iron chelation chemo-photothermal therapy. *Bioact. Mater.* **14**, 76–85 (2021).
24. M. Won *et al.*, Visible to mid IR: A library of multispectral diagnostic imaging. *Coord. Chem. Rev.* **426**, 213608 (2021).
25. M. Li *et al.*, De novo design of phototheranostic sensitizers based on structure-inherent targeting for enhanced cancer ablation. *J. Am. Chem. Soc.* **140**, 15820–15826 (2018).
26. M. Y. Li *et al.*, Quenching of singlet molecular oxygen ($^1O_2$) by azide anion in solvent mixtures. *Photochem. Photobiol.* **74**, 760–764 (2001).
27. N. Tian *et al.*, Mitochondria targeted and NADH triggered photodynamic activity of chloromethyl modified Ru(ii) complexes under hypoxic conditions. *Chem. Commun. (Camb.)* **55**, 2676–2679 (2019).
28. S. Zhang *et al.*, Unraveling and manipulating of NADH oxidation by photogenerated holes. *ACS Catal.* **10**, 4967–4972 (2020).
29. B. X. Li *et al.*, Site-selective tyrosine bioconjugation via photoredox catalysis for native-to-bioorthogonal protein transformation. *Nat. Chem.* **13**, 902–908 (2021).
30. M. Halasi *et al.*, ROS inhibitor N-acetyl-L-cysteine antagonizes the activity of proteasome inhibitors. *Biochem. J.* **454**, 201–208 (2013).
31. S. Rühl *et al.*, ESCRT-dependent membrane repair negatively regulates pyroptosis downstream of GSDMD activation. *Science* **362**, 956–960 (2018).
32. S. L. Fink, B. T. Cookson, Apoptosis, pyroptosis, and necrosis: Mechanistic description of dead and dying eukaryotic cells. *Infect. Immun.* **73**, 1907–1916 (2005).
33. B. Zhou, D. W. Abbott, Gasdermin E permits interleukin-1 beta release in distinct sublytic and pyroptotic phases. *Cell Rep.* **35**, 108998 (2021).
34. I. Noh *et al.*, Enhanced photodynamic cancer treatment by mitochondria-targeting and brominated near-infrared fluorophores. *Adv. Sci. (Weinh.)* **5**, 1700481 (2017).